Received: 10 January 2023 | Revised: 30 March 2023 | Accepted: 9 April 2023

DOI: 10.1111/ffe.14025

ORIGINAL ARTICLE

FFEMS Fatigue & Fracture of Engineering Materials & Structures WILEY

Effect of heat treatment and defects on the tensile behavior of a hot work tool steel manufactured by laser powder bed fusion

Mattia Zanni[1] | **Filippo Berto**[2,3] | **Per Erik Vullum**[4] | **Lavinia Tonelli**[1] | **Alessandro Morri**[1] | **Lorella Ceschini**[1]

[1]Department of Industrial Engineering (DIN), Alma Mater Studiorum University of Bologna, Bologna, Italy

[2]Department of Mechanical and Industrial Engineering, Norwegian University of Science and Technology (NTNU), Trondheim, Norway

[3]Department of Chemical Engineering Materials Environment, Sapienza University of Rome, Rome, Italy

[4]SINTEF Industry, Trondheim, Norway

Correspondence
Mattia Zanni, Department of Industrial Engineering (DIN), Alma Mater Studiorum University of Bologna, Viale Risorgimento 4, Bologna 40136, Italy.
Email: mattia.zanni2@unibo.it

Funding information
This research did not receive any specific grant from funding agencies in the public, commercial, or not-for-profit sectors.

Abstract

Microstructure and tensile properties of a hot work tool steel manufactured via laser powder bed fusion (LPBF) were investigated. Specimens were built under two different orientations and subjected to two quenching and tempering heat treatments, featuring different austenitizing and tempering temperatures and the eventual presence of a sub-zero step. Microstructural analyses revealed a homogeneous tempered martensite structure after both heat treatments, with the only distinction of a higher alloying segregation at a sub micrometric scale length in samples subjected to the highest tempering temperatures. Hardness and tensile tests indicated a negligible effect of building orientation on mechanical properties, but a significant influence of heat treatment parameters. The treatment featuring the lower tempering temperatures and the sub-zero step resulted in higher hardness, tensile strength, and elongation, attributed to a lower martensite tempering and alloying segregation. Tensile fracture occurred via crack initiation and unstable propagation from large LPBF defects in all the investigated conditions.

KEYWORDS

defects, heat treatment, laser powder bed fusion, mechanical properties, tool steel

Highlights

- Microstructure and tensile properties of a tool steel produced via LPBF were studied.
- Tensile failure was initiated from large defects due to the LPBF process.
- No effect of building orientation on microstructure and tensile properties was observed.
- The treatment with the lowest tempering temperatures induced the highest properties.

1 | INTRODUCTION

Tool steels are specifically designed for manufacturing equipment and thus possess high hardness and strength to avoid deformation, scratching, and indenting during service operations.[1,2] Their high hardness is achieved through an optimal combination of chemical composition and heat treatment, generally composed of austenitizing, quenching, and (multiple) tempering, which results in a tempered martensite microstructure often also containing alloying carbides. A sub-zero step can be added to the standard heat treatment procedure to reduce or eliminate the retained austenite, thus enhancing hardness, dimensional stability, and wear resistance.[2–8] In case of hot work tool steels (such as AISI H11 and H13), designed for equipment operating at high temperature, Cr, Mo, V, and W are generally alloyed beside C to improve the tempering resistance and promote the precipitation of fine tempering carbides with high hardness and good stability at the operating temperatures.[2,9,10] To ensure adequate service life, tool steels must possess high fatigue strength and duration, conferred also by an outstanding cleanliness and microstructural homogeneity. Hence, they are generally produced via special processes such as electro-slag remelting (ESR), vacuum-arc remelting, or powder metallurgy (PM). Due to these characteristics, tool steels are also suitable for the manufacturing of critical mechanical components requiring high tensile and fatigue strength, stiffness, hardness, and wear resistance, such as engine camshaft and crankshaft, in replacement of nitriding steels.[11]

Laser powder bed fusion (LPBF) is an additive manufacturing (AM) process that enables the direct manufacturing of complex near-net-shape components by selectively melting thin layers of metal powder using a laser beam as focused heat source, thus ensuring high design freedom.[12–15] The combination of design freedom ensured by LPBF, and high mechanical strength of tool steels could potentially be exploited to manufacture components with optimized geometry, high strength and low weight, enabling *lightweight* design. Although LPBF is one of the most investigated and appealing AM technologies for several engineering fields, such as automotive, aerospace and biomedical, the number of metals and alloys feasible via LPBF is still quite limited. Among steels, the LPBF process is, to date, mainly performed on alloys with low carbon content, such as maraging, austenitic, and precipitation-hardening stainless steels. On the contrary, the processing of steels with medium-to-high carbon content, such as tool steels, is still challenging since C promotes martensite formation upon rapid cooling with the consequent risk of cracking, residual stress formation and distortions.[16–19] Several literature works[20–27] reported the beneficial effect of using a preheated building plate, which dramatically reduces cracks and residual stress formation. In particular, the greatest benefit occurs at pre-heating temperatures above the *martensite start* temperature M_s, which prevent the in-process formation of martensite (around 300°C for AISI H11 and H13). LPBF also enables the possibility to develop and produce innovative composite materials by incorporating micrometric or nanometric ceramic particles into a tool steel matrix, in order to further improve their hardness, elastic modulus, and wear resistance. Literature works demonstrated the LPBF feasibility of AISI H13 hot work tool steel reinforced with TiC, TiB_2, or partially stabilized zirconia, mechanically alloyed to AISI H13 feedstock powder by high energy ball milling, describing the effect of ceramic particles on the resulting microstructure, density, and hardness.[28–30]

The second major issue is related to the microstructural features resulting from the LPBF process. As a general rule, hot work tool steels manufactured by LPBF exhibit, in the as-built condition, the typical *hierarchical* structure of most metallic LPBF parts composed of melt pool/scan track borders, columnar grains, and a fine cellular/dendritic solidification sub-structure featuring segregation of C and other alloying elements at cell boundaries, resulting from the high thermal gradient and cooling rate.[16,20,31–33] Depending on the platform preheating temperature, the as-built microstructure can be mainly martensitic or bainitic, with the eventual presence of retained austenite at cell boundaries due to C enrichment, which locally lowers the M_s temperature, stabilizing austenite at room temperature. Moreover, the LPBF process generally results in the formation of peculiar defects, such as *lack of fusion* defects (hereafter indicated as *LoF*) and gas pores, which reduce density and, most importantly, severely affect the resulting mechanical properties.[34,35] Several authors[27,33,36–40] reported the great effect of LPBF defects, in particular *lack of fusion* defects, on the mechanical properties of additively manufactured tool steels, especially on fatigue properties. Fonseca *et al*[31] reported that the choice of process parameters (such as laser power, scan speed, hatch distance, etc.) has little or no influence on the as-built microstructure of hot work tool steels but strongly affects the formation of defects. Hence, the LPBF process of hot work tool steels must be optimized aiming to minimize the content and size of LPBF defects, harmful for the mechanical behavior. Considering post-process heat treatments, previous literature works proved the possibility of obtaining high hardness and tensile strength by simply performing a direct tempering treatment after LPBF.[20,25,37,41–43] However, in view of its features, the as-built microstructure of LPBF parts is typically non-homogeneous. If more uniform characteristics are desired, a conventional heat

treatment composed of austenitizing, quenching, and (multiple) tempering, must be performed. Even so, gas pores and *lack of fusion* defects resulting from the LPBF process are still present; hence, their impact on the mechanical properties must be evaluated to assess the feasibility of hot work tool steels for the production of mechanical components by LPBF.

The aim of the present work is to investigate the effect of defects and heat treatment parameters on the mechanical properties of a hot work tool steel manufactured by LPBF. Specimens were manufactured in two different building orientations and subjected to two different heat treatments composed of austenitizing, quenching, and triple tempering, distinguished by different austenitizing and tempering temperatures and the presence or not of a sub-zero step. Mechanical properties were investigated in terms of hardness and tensile behavior and then discussed in light of the microstructural and fractographic evidences. The results were also compared with the data reported in Ceschini et al.[11] obtained on a hot work tool steel with identical composition but manufactured via ESR and previously investigated by the authors in terms of microstructure, hardness, tensile, and fatigue behavior and fracture toughness.

2 | MATERIALS & METHODS

2.1 | Specimens production and heat treatment

Specimens were supplied by Böhler Edelstahl GmbH, manufactured from the gas-atomized feedstock powder with nominal composition given in Table 1. Table 1 also reports the chemical composition of the supplied specimens checked by Glow Discharge Optical Emission Spectroscopy (GDOES) according to ISO 14707:2021, which appeared consistent with the nominal one declared by the supplier for the feedstock powder, with only little deviations in C, Cr, Mo, and V.

Cylindrical bars (ø14 mm, length 163 mm) were manufactured by LPBF using a Renishaw RenAM 500Q equipped with a building plate pre-heated at 400°C, under a high-purity argon atmosphere. Additional information on the LPBF process were not disclosed by the supplier due to industrial confidentiality reasons. To assess the effect of the building orientation, bars were manufactured along two different orientations, namely 0° and 90°. 0° bars were produced with their symmetry axis parallel to the x–y plane of laser scanning/building plate, while 90° bars were manufactured with their symmetry axis perpendicular to the building plate, as clarified in Figure 1A. 0° bars were manufactured with a prismatic support structure, not shown in Figure 1A. All the bars were subjected to a stress relief annealing at 690°C for 2 hours after the detachment from the building plate (hereafter SR condition). Specimens for tensile tests, with geometry consistent with ISO 6892 (Figure 1B), were then machined from the stress-relieved bars and, afterwards, subjected to heat treatments ("HTA" and "HTB", described in the following).

HTA and HTB treatments are schematically depicted in Figure 2. HTA included: (i) austenitizing at 1050°C in vacuum (after a double preheating at 600°C and 900°C), (ii) quenching in nitrogen gas, and (iii) triple tempering at 540–550°C. Heat treatment HTB, instead, consisted of: (i) austenitizing at 1070°C in vacuum (after the same double preheating), (ii) quenching in nitrogen gas, (iii) double tempering at 510–520°C, (iv) a sub-zero treatment at −80°C, and (v) final tempering at 520–530°C. HTA represents the standard quenching and multiple tempering treatment performed on the ESR-produced counterpart of the steel, with identical composition, previously investigated by the authors in ref.[11] Instead, the HTB treatment was designed following previous research activities performed by the authors, published in Morri et al.,[44] which indicated higher hardness, tensile strength and ductility, toughness, and fatigue strength for a PM-produced cold work tool steel subjected to a heat treatment featuring higher austenitizing temperature, lower tempering temperatures, and a − 80°C sub-zero step compared to the one subjected to the typical quenching and multiple tempering treatment.

According to building orientation and applied heat treatment, specimens were divided in four sets, as disclosed in Table 2.

2.2 | Microstructural characterization

Density, microstructure, and hardness (described in section 2.3) were evaluated on samples extracted from the

TABLE 1 Comparison between nominal chemical composition of the feedstock powder (declared by the supplier) and effective one measured on LPBF samples.

Wt.%	C	Cr	Mo	V	Si	Mn	Fe
Nominal (feedstock powder)	0.50	4.50	3.00	0.55	0.20	0.25	Bal.
Measured (LPBF samples)	0.46	4.3	3.2	0.61	0.20	0.22	Bal.

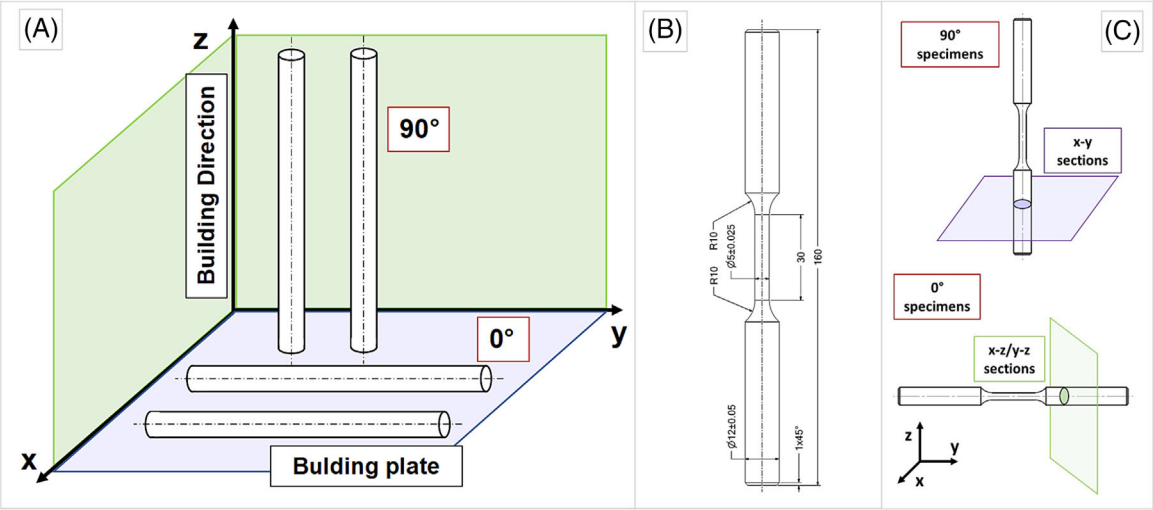

FIGURE 1 Schematic representation of bars orientation during the LPBF process (A); geometry (dimensions in mm) of tensile specimens machined form the annealed LPBF bars (B); orientation of metallographic sections extracted from 90° and 0° specimens (C). [Colour figure can be viewed at wileyonlinelibrary.com]

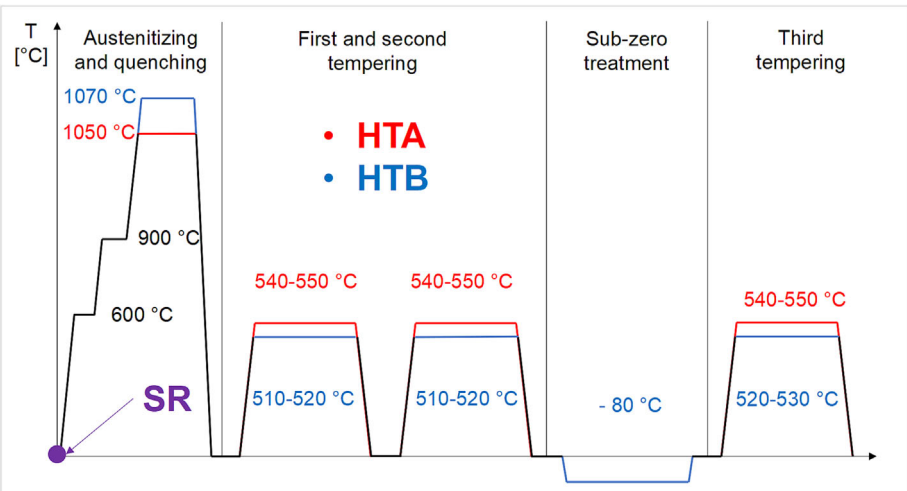

FIGURE 2 Schematic representation of heat treatments HTA and HTB. [Colour figure can be viewed at wileyonlinelibrary.com]

TABLE 2 Summary of the investigated conditions of building direction and heat treatment.

	Heat treatment	
Building orientation	**HTA**	**HTB**
90°	HTA_90°	HTB_90°
0°	HTA_0°	HTB_0°

Ø12 mm grip ends of heat-treated tensile specimens. Density measurements were performed by the gravimetric method according to the ASTM B962–17 standard using an analytical balance with 10^{-4} g precision. The relative density was calculated using the reference value of 7.85 g/cm^3, measured on the ESR produced counterpart of the steel, investigated in ref.[11] Microstructural analyses were performed on cross-sections extracted in the transverse direction respect to the specimen axis. Note that, as clarified in Figure 1C, the sections extracted from 90° specimens are parallel to the x–y plane of LPBF laser scanning/building plate, while the ones extracted from 0° specimens are normal to the x-y plane (parallel to x-z/y-z planes). Samples for metallographic analysis were prepared following the standard procedure defined in the ASTM E3–11 standard composed of hot mounting, grinding with abrasive papers up to 1,200 grit and polishing with diamond suspensions (9 μm, 3 μm, 1 μm). Low magnification images of polished sections were acquired using a Zeiss Axio Imager A.1M optical microscope (OM) and processed using the ImageJ v. 1.52a open-source software to analyze defects. Phase identification was performed using the Pananlytical X'Pert HighScore

Plus v. 2.2.0 software on X-ray diffraction (XRD) patterns acquired using a Cu-Kα source ($\lambda = 1.5405$ Å) in the 2θ range from 40° to 100°, with a 0.01° step size and a 3 s time per step. The volume content of retained austenite was calculated from the XRD patterns according to ASTM E975–22. OM analyses were performed using a Reichert metallographic microscope on sections etched with Picral Etch (4 g picric acid in 100 ml ethanol). Microstructural observations at higher magnification were performed on sections etched with Vilella's etch (1 g picric acid, 4 ml HCl, 96 ml ethanol) using a Tescan Mira 3 Field Emission Scanning Electron Microscope (SEM) equipped with energy dispersive X-ray spectroscopy (EDS) by Bruker. For comparison, XRD, OM, and SEM analyses were also performed on the material in SR condition to investigate the microstructure prior to the application of HTA and HTB heat treatments. Transmission Electron Microscopy (TEM) analyses were performed on HTA and HTB samples using a double Cs aberration corrected cold FEG JEOL ARM 200FC, operated at 200 kV, equipped with EDS and electron energy loss spectroscopy (EELS) detectors. EDS and EELS were performed simultaneously in scanning transmission electron microscopy (STEM) mode. Cross-section TEM lamellae were prepared using a FEI Helios G4 UX focused ion beam. Carbon protection layers were deposited on top of the region of interest prior to any cutting. Coarse thinning was performed with Ga^+ ions and 30 kV acceleration voltages, followed by 5 kV and 2 kV final thinning to minimize ion-beam induced surface damage. The cross-section lamellae were then cut out and transferred to dedicated Cu half grids by standard lift-out procedures.

2.3 | Mechanical characterization

Vickers hardness (HV) indentations were performed according to ISO 6507-1:2018 using a 30 Kg load on the same specimens used for metallographic analyses. Tensile tests were performed according to the ISO 6892-1:2019 standard using a servo-hydraulic testing machine, on the specimens shown in Figure 1B, for the determination of Young's modulus (E), 0.2% proof strength ($R_{P0.2}$), ultimate tensile strength (UTS), elongation after fracture (A%), and reduction of area after fracture (Z%). Three specimens were tested for each condition defined in Table 2. The strain hardening exponent (n) was calculated according to ISO 10275. Analysis of variance (ANOVA) tests with $\alpha = 0.05$ were performed on density, hardness, and tensile data using the MS Excel software to assess the effect of the investigated conditions, in terms of heat treatment and building direction, from a statistical standpoint. Fracture surfaces of tensile specimens were investigated by SEM to elucidate the mechanisms of failure.

3 | RESULTS

3.1 | Density and defects

Gravimetric measurements indicated a density of 7.826 ± 0.010 g/cm^3 and 7.832 ± 0.008 g/cm^3 for HTA and HTB specimens, respectively. ANOVA tests confirmed that no significant difference exists between HTA and HTB specimens in terms of density, in agreement with the consideration that defects, responsible of density reduction, are generated during the LPBF process. Hence, hereafter, no distinction between the two heat treatment conditions is made concerning density and defect content. The average relative density was calculated as 99.7% ± 0.12%. Figure 3A,B shows representative low magnification OM images of polished sections extracted from 90° and 0° specimens. A remarkable number of defects with size in the range 10–100 μm were observed, despite the high gravimetric density and the low area fraction of pores obtained via image analysis (0.24 ± 0.01% on x-y sections and 0.30% ± 0.11% on x-z/y-z sections). While the great part of detected defects exhibited a circular morphology, consistent with gas pores, some of them presented an irregular morphology consistent with *LoFs*. The high-magnification appearance of a *LoF* defect is reported in the SEM image in Figure 3C. Both kinds are known as typical defects resulting from the LPBF process.[12,34]

3.2 | Microstructural analyses

Figure 4 shows the microstructure in the SR condition, i.e., prior to the application of HTA or HTB heat treatments. As can be noted, in the SR condition, the steel exhibited the typical *hierarchical* structure of LPBF manufactured tool steels,[16,20,31–33] featuring melt pool borders (Figure 4A), and a cellular sub-structure resulting from alloying segregation during the rapid solidification (Figure 4C). At intermediate magnifications (Figure 4B), the microstructure appeared fully bainitic, in agreement with the prolonged isothermal exposure at 400°C during the LPBF process. In fact, as reported in Huber et al.,[45] the use of a platform pre-heating temperature higher than M_S suppresses martensite formation and promotes the isothermal transformation in bainite during the manufacturing of subsequent layers. XRD analyses (Figure 5) indicated α-ferrite as the only phase in the SR condition, with no γ-austenite nor alloying carbides resulting from the LPBF process or SR annealing.

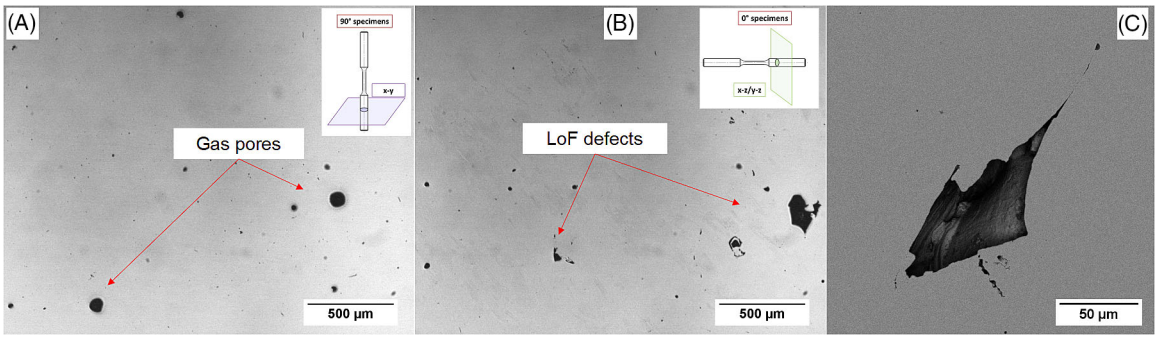

FIGURE 3 Low magnification OM images acquired from 90° (A) and 0° (B) specimens. High magnification SEM images of a *lack of fusion* defect (C). [Colour figure can be viewed at wileyonlinelibrary.com]

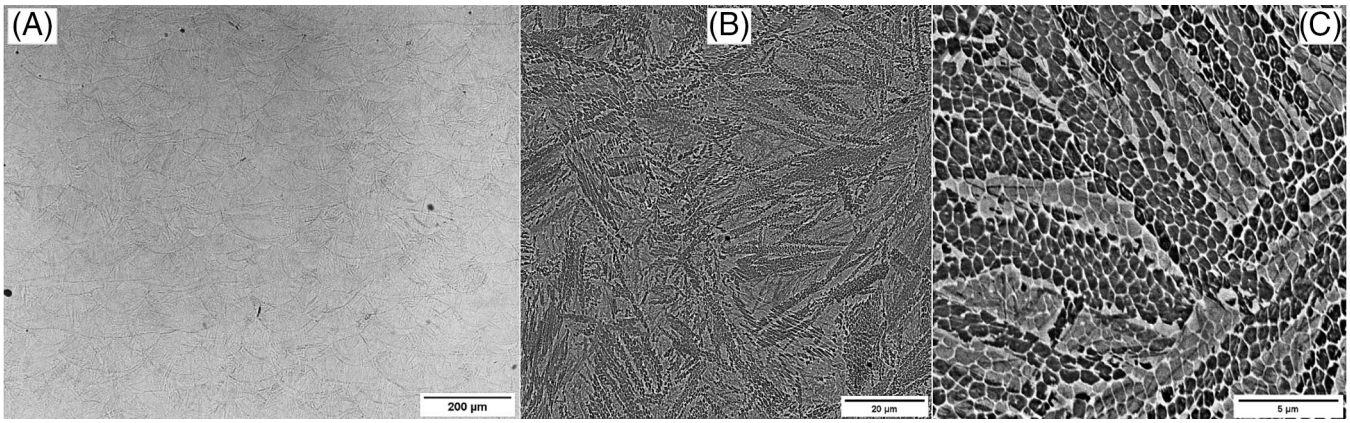

FIGURE 4 Microstructure in the SR condition: low magnification OM images (A) and back-scattered SEM images at different magnifications (B,C). [Colour figure can be viewed at wileyonlinelibrary.com]

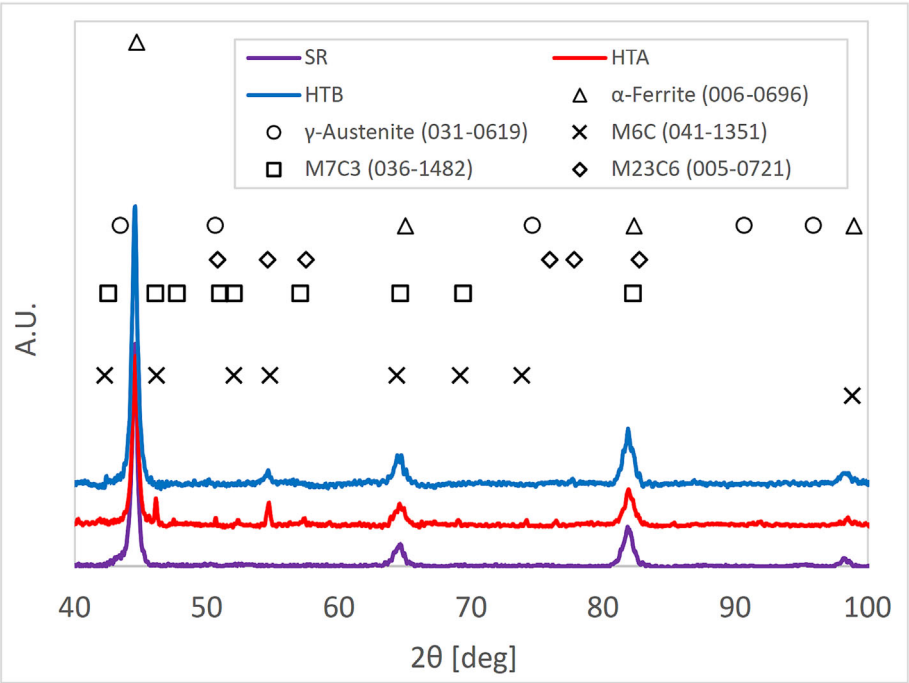

FIGURE 5 XRD patterns of specimens in the SR condition (in purple) and subjected to heat treatments HTA (in red) and HTB (in blue). [Colour figure can be viewed at wileyonlinelibrary.com]

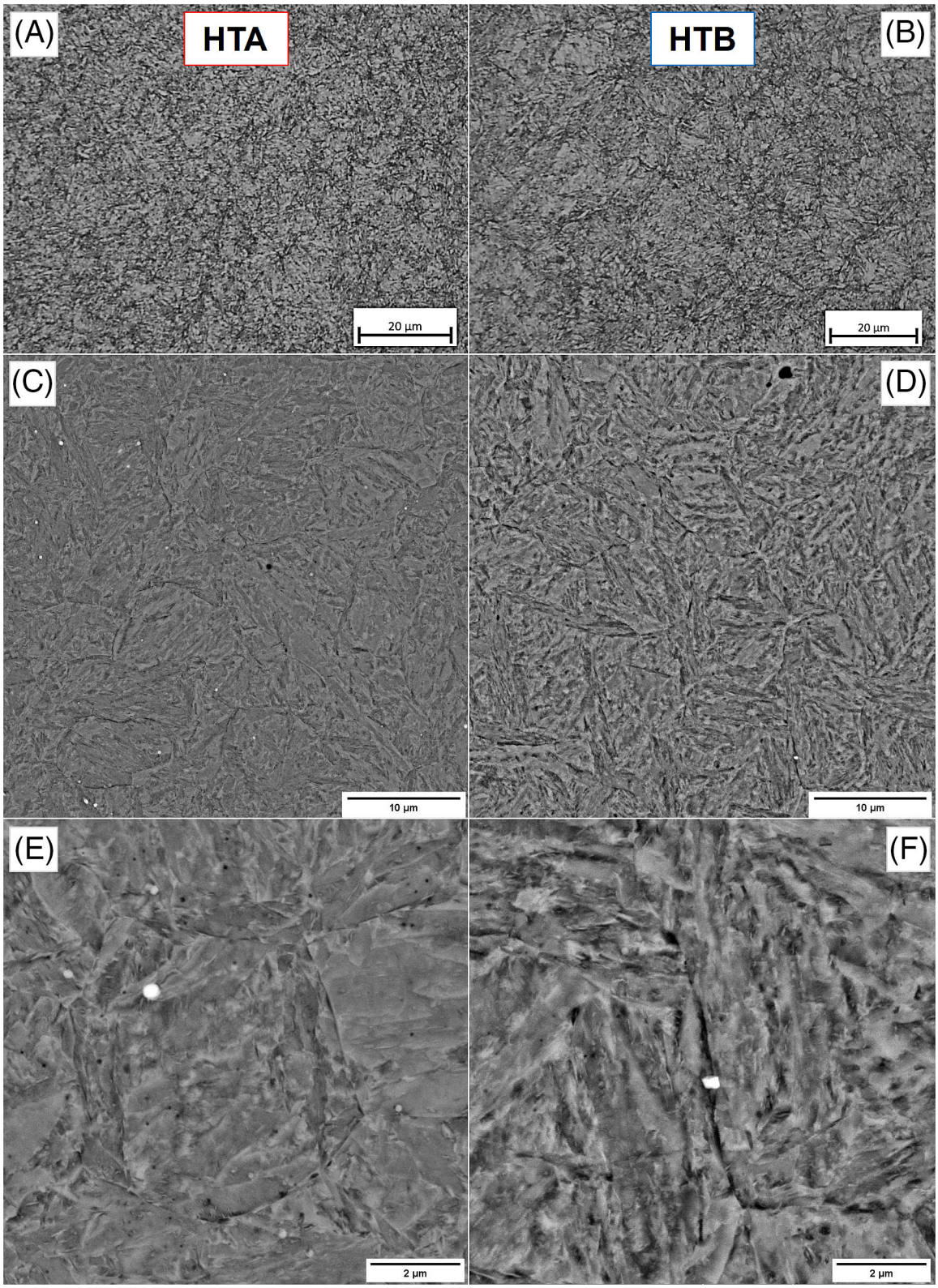

FIGURE 6 Microstructure of specimens subjected to HTA (A,C,E) and HTB (D,D,F) observed using OM (A,B) and SEM (C,D,E,F). [Colour figure can be viewed at wileyonlinelibrary.com]

For both HTA and HTB treated samples, XRD analyses indicated α-ferrite as the main phase, with negligible amounts of retained austenite below the instrumental detection limit (2%). Moreover, minor diffraction peaks were observed, possibly related to M_6C and $M_{23}C_6$ carbides, in particular for the HTA sample. M_6C and $M_{23}C_6$

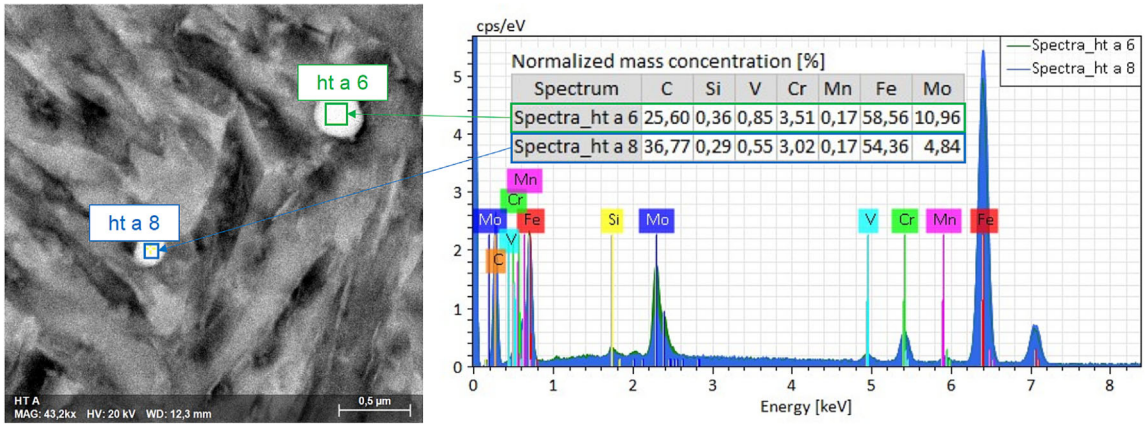

FIGURE 7 SEM-EDS composition of secondary bright particles observed in HTA specimen. [Colour figure can be viewed at wileyonlinelibrary.com]

are respectively known as typical Mo-rich and Cr-rich alloying carbides in quenched and tempered tool steels of similar composition.[2,46,47]

Figure 6 shows the microstructure of HTA and HTB specimens observed using OM and SEM in back-scattered electrons imaging (BSE). Both specimens exhibited a homogeneous tempered martensite structure, featuring equiaxed prior austenite grains with a size between 5 and 10 µm. None of the typical features of LPBF components (melt pool/scan track borders, columnar grain, cellular solidification sub-structure), still present in the SR condition, were observed, as well as differences between 90° (x-y sections) and 0° (x-z/y-z sections) specimens. High magnification SEM images (Figure 6E,F) revealed the presence of fine particles dispersed within the martensite matrix, mainly in the HTA specimens, with various appearance: i) bright particles with a size of hundreds of nm and ii) gray particles, with similar contrast to the surrounding martensite matrix and smaller than the formers. SEM-EDS analyses (Figure 7) revealed a high Mo content in bright particles, suggesting their matching with the M_6C Mo-rich carbides indicated by XRD analyses. The assessment of chemical composition of grey particles via SEM-EDS was not possible due to the size of the interaction volume between the electron beam and the sample. However, considering the atomic number contrast of BSE imaging, it is reasonable to assume that gray particles contain elements with atomic number similar to Fe ($Z = 24$), and thus probably Cr ($Z = 26$). This assumption would explain the diffraction peaks related to Cr-rich carbides from XRD patterns.

Figure 8 shows representative bright-field TEM micrographs of HTA and HTB samples and the C, Cr, Mo, and V maps of the same regions obtained via STEM-EDS and EELS. TEM analyses confirmed the presence of alloying carbides, especially in HTA samples, as indicated by the local enrichment in Mo, V, Cr, and C at the particle observed in the HTA sample. Two types of carbides were observed: Fe-based and V-based ones, also containing Mo and Cr. Both types of carbides are present, but at lower densities, in the HTB sample. Furthermore, for both types, a significant enrichment of Cr at the interface between the carbide and the steel matrix was observed. The number of carbides did not appear sufficiently high to induce an appreciable strengthening effect, neither in HTA nor in HTB samples. Considering the absence of carbides in SR samples from XRD and SEM-EDS analyses (Figures 4 and 5), it can be reasonably inferred that the ones observed in HTA and HTB samples were originated during the subsequent heat treatment, and in particular during the tempering step. For this reason, they are generally referred to as *secondary* or *tempering* carbides, in opposition to *primary* or *solidification* ones originated during steel solidification.[2] TEM analyses also indicated a segregation of Cr, Mo, and V toward the martensite laths boundaries. As for carbides, this alloying segregation appeared more pronounced in HTA samples than in HTB ones, which exhibited a more homogeneous composition.

3.3 | Mechanical properties

Table 3 summarizes hardness and tensile properties evaluated on HTA and HTB specimens. ANOVA tests indicated significant differences between HTA and HTB specimens in terms of HV, UTS, and A% but not of E and $R_{P0.2}$. Instead, the effect of the building orientation resulted non-significant for all the considered properties. Hence, tensile properties appeared substantially isotropic, in agreement with the complete absence of the LPBF hierarchical microstructure. For this reason, in the

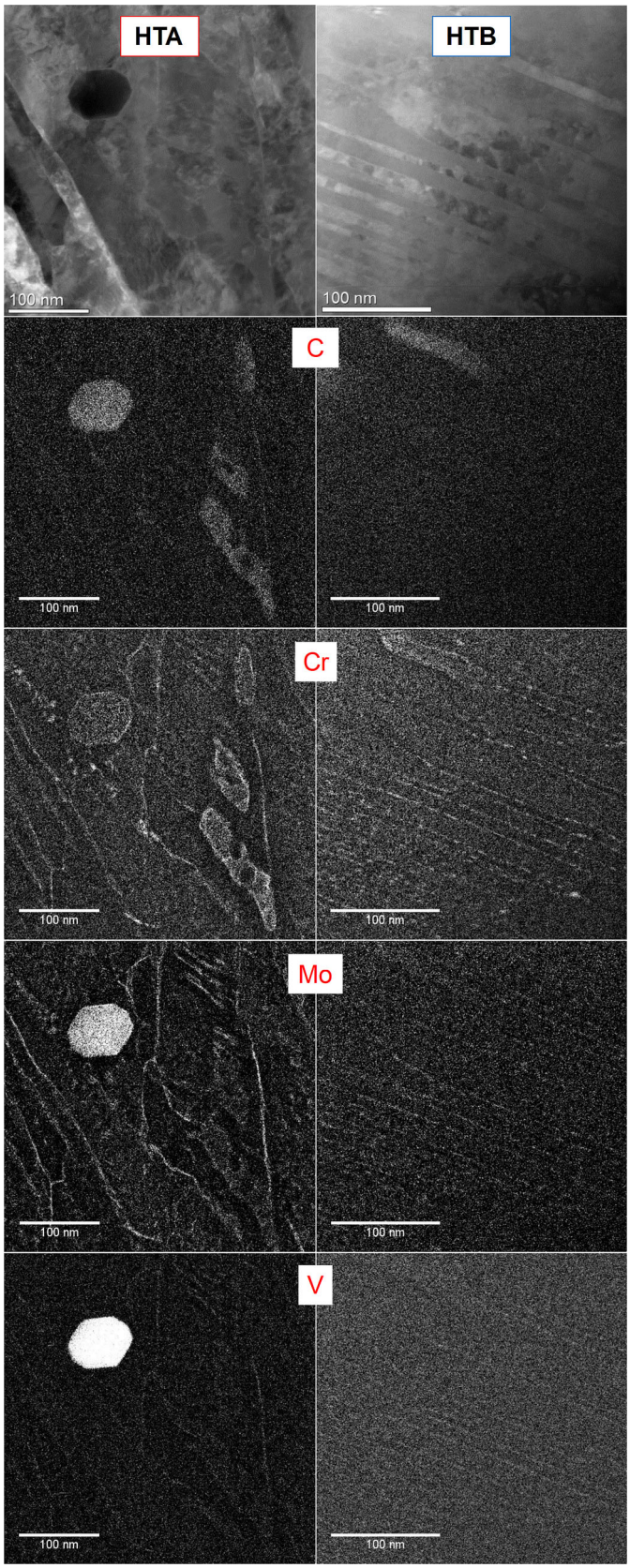

FIGURE 8 Representative TEM bright field micrographs and element maps obtained with EDS and EELS in STEM mode for HTA (left column) and HTB (right column) samples. [Colour figure can be viewed at wileyonlinelibrary.com]

following, only the effect of the heat treatment on mechanical properties will be discussed.

HTB specimens exhibited higher hardness HV (+5%), tensile strength UTS (+5%), elongation A% (+15%), and strain hardening exponent n (+29%) than HTA ones but similar proof strength $R_{P0.2}$. Due to the higher UTS for the same $R_{P0.2}$, HTB specimens exhibited a lower $R_{P0.2}$/UTS ratio (−5%). It is worth noting that, despite the higher elongation A%, HTB specimens showed a considerably lower reduction of area Z% than HTA ones (−56%). This apparently counterintuitive behavior of HTB specimens can be explained by their higher strain hardening than HTA ones, indicated by the higher n and UTS for same $R_{P0.2}$. In fact, according to previous studies,[48,49] strain hardening is a measure of the resistance opposed by the material to the localization of plastic strain (i.e. *necking*) and thus indicates the ability to withstand a large uniform plastic strain prior to the onset of necking and the subsequent fracture. Therefore, the higher strain hardening of HTB samples can explain their combination of higher elongation A% and lower area reduction Z% compared to HTA ones.

Figure 9 shows representative low magnification SEM images of the fracture surfaces of tensile specimens. The large part of tensile specimens showed a fracture morphology indicating a mechanism of unstable crack propagation initiated from a large discontinuity, which is quite unusual for ductile material subjected to tensile loading since they generally fail via *micro-voids formation and coalescence*, responsible of dimples formation and the resulting *cup-cone* fracture morphology.[48,49] The fracture was found to originate and propagate from large LPBF defects, mainly LoFs, showing an irregular morphology and large size (in the range 50–250 μm). Figure 10A shows the largest *lack of fusion* defect observed at a fracture initiation site. Besides LoFs, also gas pores or clusters of gas pores, with smaller size (approximately in the range 40–150 μm) and spherical morphology, were observed at crack origins, as shown in Figure 10B. It is worth noting that the size of defects observed at the crack initiation site widely exceeded the maximum size observed on metallographic sections (roughly 100 μm). Furthermore, many other LPBF defects randomly distributed on the fracture surfaces, mainly gas pores, were found in all the investigated specimens, consistently with metallographic observations on polished cross-sections. The fracture morphology indicated a strong influence of defects resulting from the LPBF process on the tensile mechanism and thus on tensile properties, as will be discussed in section 4. It is worth noting from Figure 9 that HTB specimens exhibited a *shear lip* considerably less wide than HTA ones. In fact, since *shear lip* is formed during

TABLE 3 Summary of hardness and tensile properties evaluated on the investigated steel manufactured by LPBF and on the ESR counterpart from ref.[11]

Condition	HV	E [GPa]	$R_{P0.2}$ [MPa]	UTS [MPa]	A% [%]	Z% [%]	n [−]
HTA_90°	636 ± 7	215 ± 7	1717 ± 25	2,165 ± 7	3.2 ± 0.1	20.7 ± 8.6	0.102
HTA_0°		208 ± 4	1729 ± 24	2,147 ± 5	3.1 ± 0.2	13.2 ± 2.0	0.102
HTB_90°	665 ± 5	215 ± 2	1719 ± 15	2,280 ± 3	3.4 ± 0.5	6.9 ± 0.4	0.133
HTB_0°		214 ± 2	1702 ± 27	2,249 ± 12	3.8 ± 0.2	8.0 ± 0.5	0.130
ESR (HTA)[11]	648–676	-	1890 ± 13	2,288 ± 11	3.1 ± 0.1	-	-

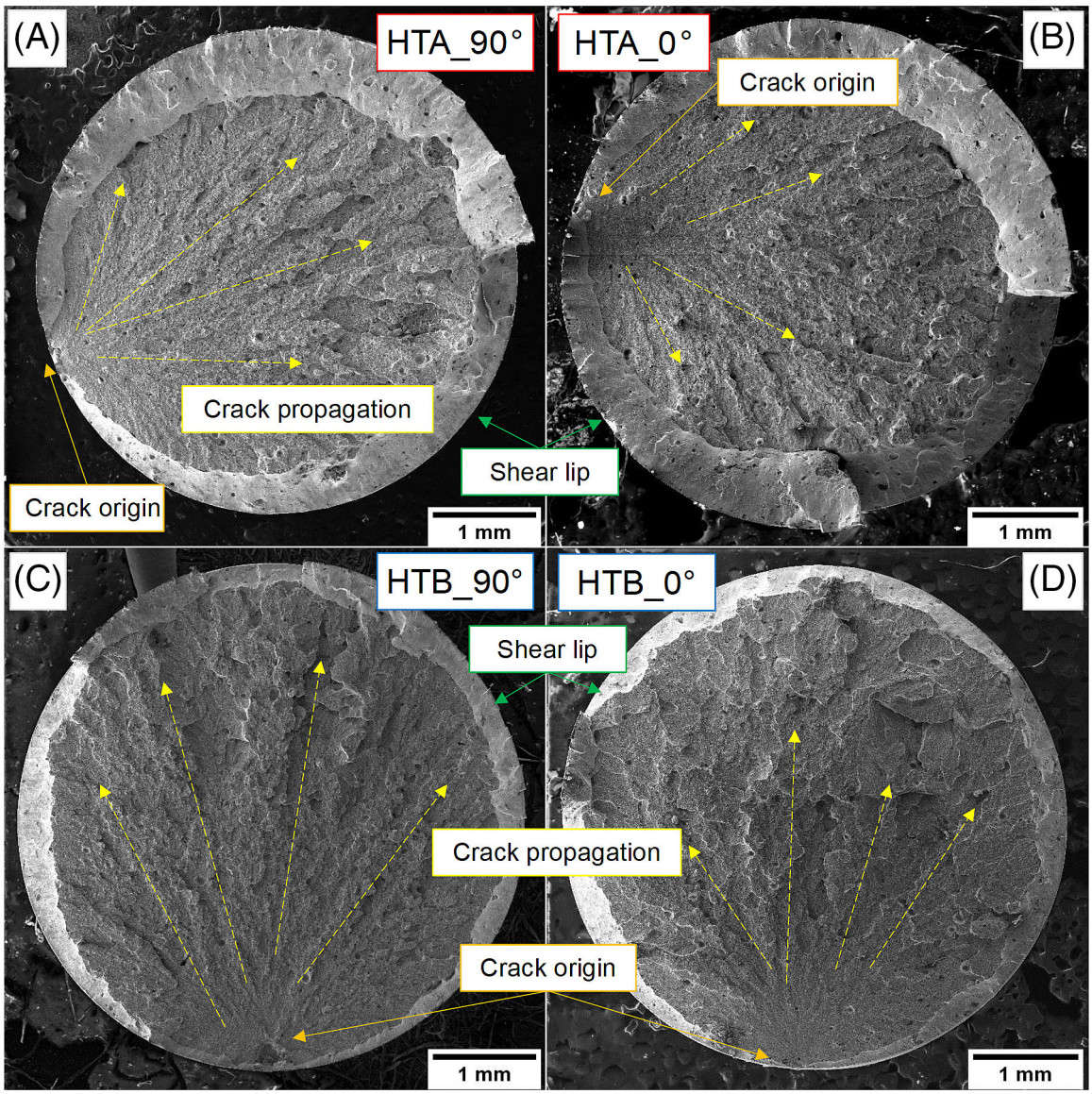

FIGURE 9 Representative low magnification SEM images of fracture surfaces of tensile specimens: HTA_90° (A), HTA_0° (B), HTB_90° (C), and HTB_0° (D). [Colour figure can be viewed at wileyonlinelibrary.com]

necking, its width is related to the area reduction Z%.[48] At higher magnification (Figure 11), the fracture surfaces showed a mixed ductile-brittle appearance composed of micron and sub-micron sized dimples and cleavage facets, consistent with unstable crack propagation in high strength martensitic steels.

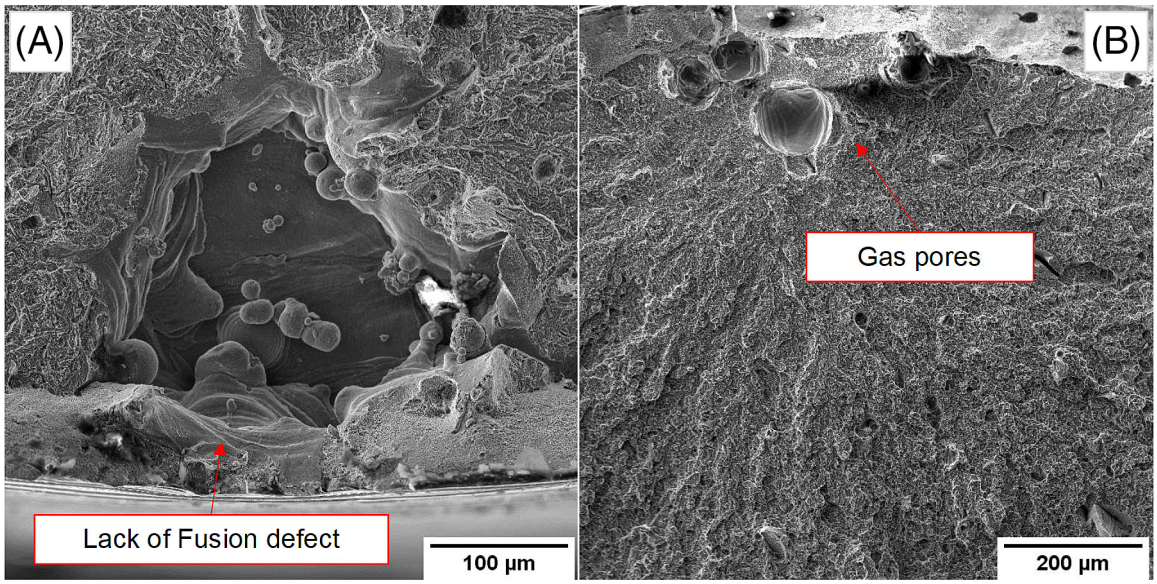

FIGURE 10 Examples of defects resulting from the LPBF process found at the crack origin of tensile specimens: (A) lack of fusion defect; (B) cluster of gas pores. [Colour figure can be viewed at wileyonlinelibrary.com]

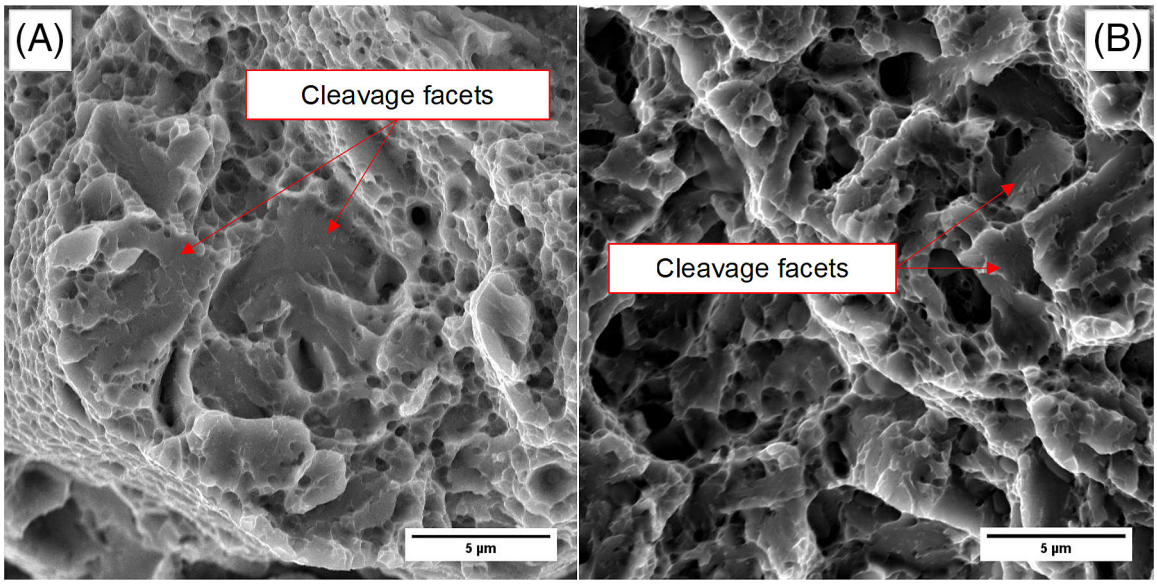

FIGURE 11 High magnification fracture morphology of tensile specimens subjected to heat treatment HTA (A) and HTB (B). [Colour figure can be viewed at wileyonlinelibrary.com]

4 | DISCUSSION

4.1 | Effect of heat treatment on microstructure and mechanical properties

The hot work tool steel investigated in the present work, manufactured via LPBF using a pre-heated platform at 400°C, exhibited, in the SR condition, the typical features of LPBF components (i.e., melt pool borders and a cellular/dendritic solidification structure resulting from the rapid solidification, as reported in ref[45]), and a fully bainitic structure consistent with the prolonged exposure at a temperature above M_s (roughly 240°C according to the formula proposed in[50]) during the LPBF process. Instead, in both HTA and HTB conditions, the microstructure appeared comparable to the one of wrought steels of similar composition, with no evidence of the typical features of as-built LPBF components, except for the peculiar defects resulting from the LPBF process (*lack of fusion* defects and gas pores). As reported in literature,[20,22,23,25,37,41,43,45,51] the lack of the typical microstructural features of LPBF components comes

from the austenitizing step, performed during HTA and HTB heat treatments. In fact, the high temperature during austenitizing promotes alloying diffusion, resulting in i) chemical homogenization, ii) removal of alloying segregation and solidification structure, and iii) recrystallization via nucleation of new austenite grains with homogeneous composition and equiaxed morphology. After quenching, a homogeneous martensitic structure is obtained, with the eventual presence of retained austenite.[20,38,41,43,45] The subsequent tempering promotes martensite tempering and softening, transformation of retained austenite, and, eventually, the precipitation of *secondary* carbides evenly distributed within the martensite matrix. As reported in section 3.2, the only microstructural distinction between HTA and HTB samples was observed on a sub-micron length scale and concerned alloying carbides and homogeneity, with HTA samples featuring precipitated carbides and a significantly higher alloying segregation at martensite inter-lath boundaries. Instead, HTB samples exhibited a more homogeneous structure, with fewer carbides and lower segregation. At the same time, mechanical tests clearly indicated an overall better behavior for specimens subjected to HTB than HTA, featuring higher hardness, UTS, and A%, thus higher tensile strength than HTA without loss of ductility. Compared to HTA, the HTB treatment features i) a slightly higher austenitizing temperature, ii) a cold treatment at −80°C between the second and third tempering, and iii) lower tempering temperatures. Traditionally, in the heat treatment of tool steels, the austenitizing temperature can be adjusted to control the amount of primary carbides solutioned and thus the amount of C and alloying elements dissolved in the austenite prior to quenching.[52] However, no carbide was observed in SR samples, thus no carbide dissolution is expected during austenitizing. Therefore, it can be reasonably inferred that the different austenitizing temperature (1,050°C for HTA vs. 1,070°C HTB) did not produce appreciable effects on the final structure and on mechanical properties. Considering the cold treatment at −80°C, according to the existing literature[3,5–8,53,54] it has the only effect of completely transform the retained austenite, eventually present after quenching, into un-tempered martensite. Theoretically, this could potentially explain the higher hardness and strength of HTB specimens than HTA. However, XRD analyses did not indicate any difference in terms of retained austenite between HTA and HTB specimens. In HTA samples, the retained austenite eventually present after quenching is completely eliminated after the triple tempering at 540–550°C. Instead, in HTB ones it is not possible to establish if the elimination of the eventual retained austenite is due to the cold treatment or if the multiple tempering is sufficient, despite the lower temperatures than in HTA. In the latter case, the −80°C cold treatment could be eliminated from HTB without penalizing the resulting mechanical properties. All considered all the observed microstructural and mechanical distinctions between HTA and HTB specimens can be explained by the different tempering temperatures. In fact, the higher hardness and tensile strength of HTB specimens can result from a lower degree of martensite tempering and softening related to the lower tempering temperatures. Moreover, the higher tempering temperature of HTA can promote alloying diffusion, with consequent higher carbide precipitation and alloying segregation than in HTB samples, which in turn can explain the lower ductility of HTA specimens.

4.2 | Effect of LPBF defects on the tensile behavior

As pointed out in section 3.2, the majority of tensile specimens exhibited a fracture morphology consistent with an unstable crack propagation mechanism, initiated from large LPBF defects. Results in section 3.1 showed that no appreciable difference exists between specimens subjected to HTA and HTB heat treatments in terms of density and defects content and characteristics. Since defects originate during the LPBF process, which is the same for all the tested specimens, it can be inferred that they are not affected by the subsequent heat treatment cycle. The typical fracture appearance of tool steels, and in general metallic materials, failed under tensile loads in absence of large defects or embrittlement phenomena, does not show crack initiation and unstable propagation but only dimples and shear lip area, resulting from the failure mechanism described in ref.[48,49] However, previous literature works addressing the tensile behavior of tool steels manufactured by LPBF[37,38,40] reported fracture surfaces similar to those observed in the present work, suggesting that process-induced defects play a key role in the fracture mechanism of these steels when manufactured via LPBF, and thus on their tensile properties. To verify the hypothesis that tensile fractures occurred via an unstable crack propagation mechanism from pre-existing LPBF defects, linear-elastic fracture mechanics (LEFM) was applied by calculating the stress intensity factor K_I at *killer* defects (i.e., observed at the crack initiation sites and thus accounted for tensile failures) using the formula $K_I = Y \cdot \sigma_0 \cdot \sqrt{\pi \cdot \sqrt{area}}$ proposed by Murakami,[55] were the term "*area*" represents the killer defect size, σ_0 the nominal applied stress and Y is a coefficient dependent on defect position (0.65 and 0.5 for surface and subsurface defects, respectively). According to LEFM, fracture occurs when the stress intensity factor K_I related to

an existing crack, defect or flaw reaches a critical value known as *fracture toughness* (K_{IC}).[56] For each specimen showing the fracture morphology reported in Figure 9, the area and position of the killer defect were measured via image analysis on the SEM images of fracture surfaces. σ_0 was calculated by dividing the maximum force applied during the tensile test to the area of the minimum cross-section after fracture, in order to correct the Ultimate Tensile Strength UTS, reported in Table 3, accounting for the effect of the little necking. The calculated values of K_I lies in the range 18–41 MPa·m$^{0.5}$ with average and standard deviation equal to 21 ± 5 MPa·m$^{0.5}$ for HTA and 28 ± 9 MPa·m$^{0.5}$ for HTB specimens. The overall average and standard deviation of K_I calculated at killer defects were equal to 26 ± 7.7 MPa·m$^{0.5}$ which, despite the large scatter, appeared reasonably comparable to the fracture toughness K_{IC} (33 ± 1.1 MPa·m$^{0.5}$) reported in ref[11] for the ESR-produced version of the steel investigated in the present work, subjected to a heat treatment consistent with HTA and possessing a similar hardness (648–676 HV), evaluated according to the ASTM E399 standard. The authors are well aware that the K_I values calculated at LPBF killer defects from fracture surfaces analyses via the procedure described above suffer from several inaccuracies and that the precise measurement of the fracture toughness K_{IC} on dedicated samples following a standard test method would be required, as performed in ref.[11] However, the similarity of K_I values calculated at *killer* defects in LPBF specimens in the present work to the fracture toughness K_{IC} calculated according to the ASTM E399 standard in ref,[11] together with the fracture appearances reported in Figures 9, 10, and 11, supports the idea that the tensile fracture of the investigated LPBF-manufactured steel occurred by unstable crack propagation from a pre-existing LPBF defect at the fulfillment of the critical condition $K_I = K_{IC}$, and thus it can be considered a *defect-controlled* phenomenon. Hence, the K_I values calculated at *killer* defects can represent a rough estimate of the fracture toughness K_{IC} of the investigated steel.

To further understand the effect of LPBF defects on the mechanical properties, HTA specimens were compared with the ESR-manufactured counterpart of the steel investigated in ref.[11] Despite the identical chemical composition and heat treatment cycle they underwent, the fracture surfaces of tensile specimens in ref[11] did not exhibit the crack propagation morphology observed in the present work, nor large defects or the mixed ductile-brittle appearance consisting of dimples and cleavage facets. Instead, they exhibited a fully ductile fracture, confirming that the peculiar fracture appearance observed in the present work is due to the presence of LPBF defects. Comparing the mechanical properties evaluated on LPBF specimens subjected to HTA treatment in present work and on the ESR steel investigated in ref[11] (Table 3), it is clear that LPBF specimens exhibited a lower hardness HV (−6%), proof strength $R_{P0.2}$ (−7%), and ultimate tensile strength UTS (−6%) than ESR ones, despite the same elongation A%. The lower hardness, proof, and tensile strength of the LPBF steel can be ascribed to the presence LPBF defects, as suggested in ref.[12,38] In fact, despite the high density (approximately 99.7%), the investigated LPBF specimens contained a high number of defects resulting from the LPBF process, with a size ranging from tenth to hundreds of μm. As in porous and sintered materials, these defects reduce the *effective load-bearing section* with respect to the nominal cross section, thus reducing the resulting mechanical properties.[57] However, no ductility reduction (in terms of A%) was observed. According to ref,[15,58] defects possess a detrimental effect on fatigue, toughness, and ductility properties. On the opposite, different authors[12,15,59] claim that LPBF components can possess a higher ductility than conventional ones due to their finer microstructure resulting from the high cooling rates, despite defects. It follows that no general rule regarding the ductility of LPBF components compared to the counterparts produced via conventional manufacturing processes can be drawn. In conclusion, it appears possible that the fine microstructure resulting from the LPBF process, even after the performed heat treatments, can counterbalance the eventual ductility loss due to LPBF defects.

5 | CONCLUSIONS

In the present work, the microstructure, hardness, and tensile properties of a hot work tool steel, manufactured by LPBF along two different building orientations (0° and 90°) and subjected to two different heat treatments (HTA and HTB) were investigated. Compared to HTA, HTB featured a slightly higher austenitizing temperature, lower tempering temperatures, and a cold treatment. The following conclusions can be drawn:

- A homogeneous tempered martensite structure was observed in both HTA and HTB samples. The only differences concerned higher alloying segregation and precipitated carbides in HTA samples due to the higher tempering temperature.
- Specimens subjected to HTB treatment exhibited higher hardness, tensile strength, and elongation due to the lower martensite tempering, alloying segregation, and carbide precipitation resulting from the lower tempering temperatures.

- No significant effect of the building orientation on microstructure and mechanical properties after heat treatment was observed.
- Fracture surfaces exhibited a "crack-propagation" morphology, initiated from large LPBF defects (typically *lack of fusion* defects). The stress intensity factor K_I at the *killer* defect appeared consistent with literature data for the fracture toughness K_{IC} of the ESR counterpart of the steel.
- Compared to literature data for the ESR counterpart, the LPBF-manufactured steel exhibited lower hardness and strength due to the presence of defects, but similar elongation. It was suggested that the fine structure resulting from LPBF could counterbalance the detrimental effect of defects.

AUTHOR CONTRIBUTIONS

All authors contributed to the study conception and design. Material preparation, data collection and analysis were performed by Mattia Zanni, Per Erik Vullum, and Lavinia Tonelli. The first draft of the manuscript was written by Mattia Zanni and all authors commented on previous versions of the manuscript. All authors read and approved the final manuscript.

ACKNOWLEDGMENTS

The authors thank Dr. Simone Messieri at Ducati Motor Holding S.p.A. for his valuable support to the experimental work and the fruitful discussion. Open Access Funding provided by Universita degli Studi di Bologna within the CRUI-CARE Agreement.

CONFLICT OF INTEREST STATEMENT

The Authors declare that they have no competing interest to disclose.

DATA AVAILABILITY STATEMENT

The data required to reproduce the findings reported in the present work are available in the diagrams, tables, and images of this manuscript.

ORCID

Mattia Zanni https://orcid.org/0000-0002-3992-0037
Filippo Berto https://orcid.org/0000-0001-9676-9970
Per Erik Vullum https://orcid.org/0000-0001-7968-4879
Lavinia Tonelli https://orcid.org/0000-0002-6014-2233
Alessandro Morri https://orcid.org/0000-0002-7062-2951
Lorella Ceschini https://orcid.org/0000-0003-2358-1306

REFERENCES

1. Zanni M, Morri A, Ceschini L. Development and validation of a probabilistic model for notch fatigue strength prediction of tool steels based on surface defects. *Fatigue Fract Eng Mater Struct*. 2022;45(1):113-132.
2. Roberts G, Krauss G, Kennedy R. *Tool Steels*. 5th Edition. Book ed; 1998:121.
3. Das D, Dutta AK, Ray KK. Correlation of microstructure with wear behaviour of deep cryogenically treated AISI D2 steel. *Wear*. 2009;267(9-10):1371-1380.
4. Das D, Dutta AK, Ray KK. Sub-zero treatments of AISI D2 steel: part I. Microstructure and hardness. *Mater Sci Eng A*. 2010;527(9):2182-2193.
5. Das D, Sarkar R, Dutta AK, Ray KK. Influence of sub-zero treatments on fracture toughness of AISI D2 steel. *Mater Sci Eng A*. 2010;528(2):589-603.
6. Çakir FH, Çelik ON. The effects of cryogenic treatment on the toughness and tribological behaviors of eutectoid steel. *J Mech Sci Technol*. 2017;31(7):3233-3239.
7. Gavriljuk VG, Theisen W, Sirosh VV, et al. Low-temperature martensitic transformation in tool steels in relation to their deep cryogenic treatment. *Acta Mater*. 2013;61(5):1705-1715.
8. Diekman F. Cold and cryogenic treatment of steel. In: *Steel Heat Treating Fundamentals and Processes*. ASM International; 2013:382-386.
9. Davis JR (Ed). Tool steels. In: *Metals Handbook Desk Edition*. Second Edi. ed. ASM International; 1998:346-361.
10. Mesquita RA, Schneider R, Gonçalves CS. Heat treating of hot-work tool steels. In: *Heat Treating of Irons and Steels*. ASM International; 2014:336-346.
11. Ceschini L, Morri A, Morri A, Messieri S. Replacement of nitrided 33CrMoV steel with ESR hot work tool steels for motorsport applications: microstructural and fatigue characterization. *J Mater Eng Perform*. 2018;27(8):3920-3931
12. DebRoy T, Wei HL, Zuback JS, et al. Additive manufacturing of metallic components – process, structure and properties. *Prog Mater Sci*. 2018;92:112-224.
13. Yap CY, Chua CK, Dong ZL, et al. Review of selective laser melting: materials and applications. *Appl Phys Rev*. 2015;2(4):041101.
14. Hebert RJ. Viewpoint: metallurgical aspects of powder bed metal additive manufacturing. *J Mater Sci*. 2016;51(3):1165-1175.
15. Herzog D, Seyda V, Wycisk E, Emmelmann C. Additive manufacturing of metals. *Acta Mater*. 2016;117:371-392.
16. Bajaj P, Hariharan A, Kini A, Kürnsteiner P, Raabe D, Jägle EA. Steels in additive manufacturing: a review of their microstructure and properties. *Mater Sci Eng A*. 2020;772:138633.
17. Haghdadi N, Laleh M, Moyle M, Primig S. Additive manufacturing of steels: a review of achievements and challenges. *J Mater Sci*. 2021;56(1):64-107.
18. Fayazfar H, Salarian M, Rogalsky A, et al. A critical review of powder-based additive manufacturing of ferrous alloys: process parameters, microstructure and mechanical properties. *Mater des*. 2018;144:98-128.
19. Campbell CE, Stoudt MR, Zhang F. Additive manufacturing of steels and stainless Steels. In: *Additive Manufacturing Processes*. ASM International; 2020:346-365.
20. Krell J, Röttger A, Geenen K, Theisen W. General investigations on processing tool steel X40CrMoV5-1 with selective laser melting. *J Mater Process Technol*. 2018;255:679-688.

21. Agapovichev AV, Sotov AV, Kyarimov RR, et al. The investigation of microstructure and mechanical properties of tool steel produced by selective laser melting technology. *IOP Conf Ser Mater Sci Eng*. 2018;441:012003.
22. Boes J, Röttger A, Mutke C, Escher C, Theisen W. Microstructure and mechanical properties of X65MoCrWV3-2 cold-work tool steel produced by selective laser melting. *Addit Manuf*. 2018;23:170-180.
23. Narvan M, Al-Rubaie KS, Elbestawi M. Process-structure-property relationships of AISI H13 tool steel processed with selective laser melting. *Materials (Basel)*. 2019;12(14):2284.
24. He Y, Zhong M, Beuth J, Webler B. A study of microstructure and cracking behavior of H13 tool steel produced by laser powder bed fusion using single-tracks, multi-track pads, and 3D cubes. *J Mater Process Technol*. 2020;286:116802.
25. Wang M, Li W, Wu Y, et al. High-temperature properties and microstructural stability of the AISI H13 hot-work tool steel processed by selective laser melting. *Metall Mater Trans B*. 2019;50(1):531-542.
26. Wu L, Das S, Gridin W, et al. Hot work tool steel processed by laser powder bed fusion: a review on most relevant influencing factors. *Adv Eng Mater*. 2021;23(7):2100049.
27. Mertens R, Vrancken B, Holmstock N, Kinds Y, Kruth J-P, Van Humbeeck J. Influence of powder bed preheating on microstructure and mechanical properties of H13 tool steel SLM parts. *Phys Procedia*. 2016;83:882-890.
28. AlMangour B, Grzesiak D, Yang J-M. Nanocrystalline TiC-reinforced H13 steel matrix nanocomposites fabricated by selective laser melting. *Mater des*. 2016;96:150-161.
29. AlMangour B, Grzesiak D, Yang J-M. Selective laser melting of TiB 2/H13 steel nanocomposites: influence of hot isostatic pressing post-treatment. *J Mater Process Technol*. 2017;244:344-353.
30. Deirmina F, AlMangour B, Grzesiak D, Pellizzari M. H13–partially stabilized zirconia nanocomposites fabricated by high-energy mechanical milling and selective laser melting. *Mater des*. 2018;146:286-297.
31. Fonseca EB, Gabriel AHG, Araújo LC, Santos PLL, Campo KN, Lopes ESN. Assessment of laser power and scan speed influence on microstructural features and consolidation of AISI H13 tool steel processed by additive manufacturing. *Addit Manuf*. 2020;34:101250.
32. Lei F, Wen T, Yang F, et al. Microstructures and mechanical properties of H13 tool steel fabricated by selective laser melting. *Materials (Basel)*. 2022;15(7):2686.
33. Wang J, Liu S, Fang Y, He Z. A short review on selective laser melting of H13 steel. *Int J Adv Manuf Technol*. 2020;108(7-8):2453-2466.
34. Mostafaei A, Zhao C, He Y, et al. Defects and anomalies in powder bed fusion metal additive manufacturing. *Curr Opin Solid State Mater Sci*. 2022;26(2):100974.
35. Platl J, Leitner H, Turk C, Demir AG, Previtali B, Schnitzer R. Defects in a laser powder bed fused tool steel. *Adv Eng Mater*. 2021;23(12):2000833.
36. Mazur M, Brincat P, Leary M, Brandt M. Numerical and experimental evaluation of a conformally cooled H13 steel injection mould manufactured with selective laser melting. *Int J Adv Manuf Technol*. 2017;93(1-4):881-900.
37. Åsberg M, Fredriksson G, Hatami S, Fredriksson W, Krakhmalev P. Influence of post treatment on microstructure, porosity and mechanical properties of additive manufactured H13 tool steel. *Mater Sci Eng A*. 2019;742:584-589.
38. Lee J, Choe J, Park J, et al. Microstructural effects on the tensile and fracture behavior of selective laser melted H13 tool steel under varying conditions. *Mater Charact*. 2019;155:109817.
39. Oliveira AP, Lima LHQR, Felipe BCA, Bolfarini C, Coelho RT, Gargarella P. Effect of microstructure and defect formation on the bending properties of additive manufactured H13 tool steel. *J Mater Res Technol*. 2021;15:3598-3609.
40. Vilardell AM, Hosseini SB, Åsberg M, et al. Evaluation of post-treatments of novel hot-work tool steel manufactured by laser powder bed fusion for aluminum die casting applications. *Mater Sci Eng A*. 2021;800:140305.
41. Casati R, Coduri M, Lecis N, Andrianopoli C, Vedani M. Microstructure and mechanical behavior of hot-work tool steels processed by selective laser melting. *Mater Charact*. 2018;137:50-57.
42. Junker D, Hentschel O, Schmidt M, Merklein M. Investigation of heat treatment strategies for additively-manufactured tools of X37CrMoV5-1. *Metals (Basel)*. 2018;8(10):854.
43. Deirmina F, Peghini N, AlMangour B, Grzesiak D, Pellizzari M. Heat treatment and properties of a hot work tool steel fabricated by additive manufacturing. *Mater Sci Eng A*. 2019;753:109-121.
44. Morri A, Ceschini L, Messieri S. Effect of different heat treatments on tensile properties and Unnotched and notched fatigue strength of cold work tool steel produced by powder metallurgy. *Metals (Basel)*. 2022;12(6):900.
45. Huber F, Bischof C, Hentschel O, et al. Laser beam melting and heat-treatment of 1.2343 (AISI H11) tool steel – microstructure and mechanical properties. *Mater Sci Eng A*. 2019;742:109-115.
46. Kang M, Park G, Jung J-G, Kim B-H, Lee Y-K. The effects of annealing temperature and cooling rate on carbide precipitation behavior in H13 hot-work tool steel. *J Alloys Compd*. 2015;627:359-366.
47. Ning A, Mao W, Chen X, Guo H, Guo J. Precipitation behavior of carbides in H13 hot work die steel and its strengthening during tempering. *Metals (Basel)*. 2017;7(3):70.
48. McGarry D. Mechanisms and appearances of ductile and brittle fracture in metals. In: Miller BA, Shipley RJ, Parrington RJ, Dennies DP, eds. *ASM Handbook*. Failure Analysis and Prevention. Vol.11. ASM International; 2021:304-342.
49. Dieter GE. Mechanical behavior under tensile and compressive loads. In: Kuhn H, Medlin D, eds. *ASM Handbook*. Mechanical Testing and Evaluation. Vol.8. ASM International; 2000:99-108.
50. Barbier D. Extension of the Martensite transformation temperature relation to larger alloying elements and contents. *Adv Eng Mater*. 2014;16(1):122-127.
51. Pellizzari M, Furlani S, Deirmina F, Siriki R, AlMangour B, Grzesiak D. Fracture toughness of a hot work tool steel fabricated by laser-powder bed fusion additive manufacturing. *Steel Res Int*. 2020;91(5):1900449.
52. Bignozzi MC, Calcinelli L, Carati M, et al. Effect of heat treatment conditions on retained austenite and corrosion resistance

of the X190CrVMo20-4-1 stainless steel. *Met Mater Int*. 2019; 26(9):1318-1328.
53. Senthilkumar D, Rajendran I, Pellizzari M, Siiriainen J. Influence of shallow and deep cryogenic treatment on the residual state of stress of 4140 steel. *J Mater Process Technol*. 2011; 211(3):396-401.
54. Baldissera P, Delprete C. Deep cryogenic treatment: a bibliographic review. *Open Mech Eng J*. 2008;2(1):1-11.
55. Murakami Y. *Metal Fatigue*. Elsevier; 2002.
56. Anderson TL. *Fracture Mechanics*. CRC Press; 2017.
57. Dos Santos DT, Salemi A, Cristofolini I, Molinari A. The tensile properties of a powder metallurgy Cu–Mo–Ni diffusion bonded steel sintered at different temperatures. *Mater Sci Eng A*. 2019; 759:715-724.
58. Mashl SJ. Powder metallurgy processing by hot isostatic pressing. In: *Powder Metallurgy*. ASM International; 2015:260-270.
59. Frazier WE. Metal additive manufacturing: a review. *J Mater Eng Perform*. 2014;23(6):1917-1928.

How to cite this article: Zanni M, Berto F, Vullum PE, Tonelli L, Morri A, Ceschini L. Effect of heat treatment and defects on the tensile behavior of a hot work tool steel manufactured by laser powder bed fusion. *Fatigue Fract Eng Mater Struct*. 2023;46(7):2681-2696. doi:10.1111/ffe.14025